Available online at www.sciencedirect.com
ScienceDirect
Magnetic Resonance Imaging 26 (2008) 1133–1144
MAGNETIC RESONANCE IMAGING

Variational multiple-tensor fitting of fiber-ambiguous diffusion-weighted magnetic resonance imaging voxels

Ofer Pasternak[a,*], Yaniv Assaf[c,d], Nathan Intrator[a], Nir Sochen[b]

[a]School of Computer Science, Tel Aviv University, Tel Aviv 69978, Israel
[b]Department of Applied Mathematics, Tel Aviv University, Tel Aviv 69978, Israel
[c]Faculty of Life Sciences, Department of Neurobiology, Tel Aviv University, Tel Aviv 69978, Israel
[d]The Functional Brain Imaging Unit, Tel Aviv Sourasky Medical Center, Tel Aviv 64239, Israel

Received 6 April 2007; revised 23 December 2007; accepted 6 January 2008

Abstract

Partial volume effects are often experienced in diffusion-weighted MRI of biologic tissue. This is when the signal attenuation reflects a mixture of diffusion processes, originating from different tissue compartments, residing in the same voxel. Decomposing the mixture requires elaborated models that account for multiple compartments, yet the fitting problem for those models is usually ill posed. We suggest a novel approach for stabilizing the fitting problem of the multiple-tensors model by a variational framework that adds biologically oriented assumption of neighborhood alignments. The framework is designed to address fiber ambiguity caused by a number of neuronal fiber compartments residing in the same voxel. The method requires diffusion data acquired by common, clinically feasible MRI sequences, and is able to derive familiar tensor quantities for each compartment. Neighborhood alignment is performed by adding piece-wise smooth regularization constraints to an energy function. Minimization with the gradient descent method produces a set of diffusion-reaction partial differential equations that describe a tensor-preserving flow towards a best approximation of the data while maintaining the constraints. We analyze fiber compartment separation capabilities on a synthetic model of crossing fibers and on brain areas known to have crossing fibers. We compare the results with diffusion tensor imaging analysis and discuss applications for the framework.
© 2008 Elsevier Inc. All rights reserved.

Keywords: Diffusion tensor; Variational model regularization; Partial volume; Crossing fibers; Ill-posed inverse problem

1. Introduction

Diffusion-weighted MRI (DW-MRI) measures the apparent water molecules' self-diffusion along a direction determined by the applied gradient [1]. To date, diffusion tensor imaging (DTI) is the most popular clinical and research tool for analyzing diffusion-weighted images (DWIs), thanks to its ability to segment organized white matter bundles [2]. The DTI model, however, is not accurate in areas of complex architecture [3], where partial volume effects occur. The model is based on a solution for the diffusion equations that sets boundary conditions of a single nonrestricted and homogenous compartment. Molecule displacement is then expected to be normally distributed; fully described by a single, second-order, symmetric and positive definite diffusion tensor, D; and related to the normalized attenuation signal, E, by the simple relation [2]

$$E(q_k) = \frac{A(q_k)}{A(0)} = exp\left(-bq_k^{\mathrm{T}} D q_k\right). \quad (1)$$

Here $A(q_k)$ is a DWI for the kth applied diffusion gradient direction q_k. The notation $A(0)$ stands for the nonweighted image and b is a constant reflecting the experimental diffusion weighting [4]. A second-order symmetric tensor has a spectral decomposition

$$D = \sum_{a=1}^{3} \lambda_a U_a (U_a)^{\mathrm{T}}, \quad (2)$$

for three eigenvectors U_a and three positive eigenvalues λ_a. The relation between the eigenvalues determines the

* Corresponding author.
E-mail address: oferpas@tau.ac.il (O. Pasternak).

0730-725X/$ – see front matter © 2008 Elsevier Inc. All rights reserved.
doi:10.1016/j.mri.2008.01.006

diffusion anisotropy, using measures such as fractional anisotropy (FA) [5]:

$$\mathrm{FA}=\sqrt{\frac{3\left((\lambda_1-\langle D\rangle)^2+(\lambda_2-\langle D\rangle)^2+(\lambda_3-\langle D\rangle)^2\right)}{2\left(\lambda_1^2+\lambda_2^2+\lambda_3^2\right)}}, \quad (3)$$

where $\langle D\rangle=(\lambda_1+\lambda_2+\lambda_3)/3$. It was experimentally shown that diffusion in voxels containing homogeneous white matter is best fitted with cigar-shaped ellipsoids ($\lambda_1\gg\lambda_2\simeq\lambda_3$) [3]. Such tensors have high FA, whereas other brain tissue, namely, gray matter and cerebrospinal fluid (CSF), is best fitted with isotropic, low FA tensors [3]. Moreover, the principal eigenvectors of cigar-shaped tensors in white matter voxels were found to be aligned with the underlying fiber orientation [3]. This is the basis for tractography, which use the eigenvector orientation field in order to infer connectivity between brain areas [6].

Partial volume effects in DWIs occur where attenuation within a voxel originates from different compartments with different diffusion profiles. Specifically for brain images, partial volume appears where different tissue types reside in the same voxel [7]. Setting homogeneous compartment boundary conditions for a partial volume voxel results in a tensor solution that models a mixture of all compartments [8]. For the case where neuronal fiber tissue has partial volume with another tissue, the tensor often deviates from the typical cigar shape to have an oblate shape ($\lambda_1\simeq\lambda_2\gg\lambda_3$), or even a spherical shape ($\lambda_1\simeq\lambda_2\simeq\lambda_3$) [8,9]. Fiber ambiguity is when the neuronal fiber tissue shares the voxel with other neuronal fiber tissues. The fitted tensor to a fiber ambiguous voxel has principal orientation not necessarily aligned with any fiber orientation, and a low FA value [7]. This makes it harder to segment the voxel as a white matter voxel and creates a deviation in tracts obtained by tractography [6].

Extensive research has been undertaken in the past few years to resolve partial volume effects and specifically to solve the fiber ambiguity problem. Some approaches are model based, with diffusion models that account for multiple compartments (e.g., Refs. [8,10]). Other approaches are model free and concentrate on extracting the angular structure of the diffusion distribution (e.g., Refs. [11–14]). Model-free methods enhance the directionality of the diffusion profile and then detect peaks in the predicted probability density function (PDF) that describes the enhanced profile. Fiber orientations are then expected to be parallel to the found peaks. In the process of directionality enhancement, often the shape of the predicted compartment is changed, and therefore other properties of fiber compartments (such as anisotropy, width or volume) are harder to find. All model-based approaches share the property that the more sophisticated the model, the more free parameters it has to assess and the more difficult the inverse problem solution becomes. A comprehensive review and comparison of both model-based and model-free approaches can be found in Ref. [15]. All methods require an increasing number of applied gradient orientations and increasing sensitivity in terms of higher b values. The method proposed here suggests, and demonstrates, that the fitting problem of model-based methods can be stabilized by adding neighborhood alignment constraints. The framework we offer is applied on the multiple-tensors model, which is a straightforward generalization of the DTI model and is the simplest model that accounts for voxels comprising a number of different compartments. As such, data acquisition is similar to clinically used sequences, does not require high b values and enhances the compartment separation abilities of the fitting.

In the next section, we will elaborate on the theoretical aspects of variational regularization along with a detailed description of the framework and its implementation for the chosen diffusion model. In Section 3, we will describe the experimental setup, chosen parameters and visualization techniques used. In Section 4, we will present compartment separation results for a synthetic data and for human data. We will also demonstrate how to use the outcome of our method in order to perform tractography. We will further discuss our findings in Section 5, concentrating on what our framework has achieved for different brain tissue types and its value for future applications. We conclude by summarizing our findings.

2. Theory

Variational methods in the context of DW-MRI were mainly proposed as a denoising mechanism. A variational framework solves inverse (ill-posed) problems by defining a functional over the space of states, e.g., possible approximations for the data. Minimizing the functional by a gradient descent method characterizes the best state as a solution to some partial differential equations (PDEs). These PDEs describe a "flow" of states towards the best one [16]. The functionals share the general form:

$$F(I)=\int_{\Omega}(\alpha M(I,I_0)+R(\nabla I))\mathrm{d}\Omega\,, \quad (4)$$

for some initial state I_0 out of all states' domain Ω. The minimum of F is achieved with an optimal state I. The functional consists of two terms: the data attachment term, governed by some function M, and the regularization term, governed by some function R. The relative effect of these terms is defined by the scalar α. The PDEs are defined by solving the Euler–Lagrange equations for the functional. Variational methods were used for DWI denoising [17,18], as a denoising operator for tensor fields [19], and for simultaneous fitting and smoothing of tensor fields [20–22]. These methods differ mainly by the functions R and M, and by different approaches to preserve the tensor attributes during the flow. A comparison between variational methods

can be found in Ref. [23]. The framework we propose here differs from the methods mentioned above in its purpose. We apply regularization as a way to allow separation of diffusion compartments rather than smoothing the tensor field. Nevertheless, smoothing is a welcomed by-product of the method and is obtained simultaneously with the model fitting. A variational framework for fiber compartment separation was also proposed in Ref. [24], although there the fitting was done using pre-chosen tensor basis, and the smoothing was done by the variation of the basis coefficients.

2.1. Multiple diffusion tensors model

Since the DTI model is not sufficient for voxels with partial volume effects, we chose the multiple diffusion tensors (MDT) model [8,25], which is the simplest model that accounts for voxel heterogeneity. The MDT model assumes a discrete number of homogeneous regions comprising each voxel. The compartments are assumed to have slow exchange, i.e., separated by a distance much greater than the diffusion mixing length. It is further assumed that molecule displacement within each region has a Gaussian distribution, i.e., can be fully described by a tensor. Under those assumptions the diffusion profile of any compartment is independent of diffusion profiles of other compartments, and each compartment holds DTI assumptions. Therefore, MDT models the signal attenuation with finite mixture of n components:

$$E(D,f,q_k)=\sum_{i=1}^{n} f_i E_i(D_i,q_k), \tag{5}$$

with each component described as

$$E_i(D_i,q_k)=exp\left(-bq_k^{\mathrm{T}}D_iq_k\right), \tag{6}$$

where f_i is the relative weight of E_i, the ith component in the mixture. To ensure that the volume fractions are properly bounded ($f_i\in[0,1]$) and normalized ($\sum_i f_i = 1$), the weights are calculated through the soft-max transform

$$f_i(\eta)=\frac{e^{\eta_i}}{\sum_{j=1}^{n} e^{\eta_j}}, \tag{7}$$

where $\eta_i\in\mathbb{R}$. With the use of Eqs. (2) and (7), the modeled signal can take the form:

$$E(\eta,\lambda,U,q_k)=\sum_{i=1}^{n} f_i(\eta)exp\left(-bq_k^{\mathrm{T}}\left(\sum_{a=1}^{3}(\lambda_a)_i(U_a)_i(U_a)_i^{\mathrm{T}}\right)q_k\right), \tag{8}$$

where $(\lambda_a)_i$ ((U_a))$_i$ is the ath eigenvalue (eigenvector) of the ith diffusion tensor. The inverse problem of MDT fitting is the attempt to find a best multiple-tensors field with matching weights for a given measured signal, $\hat{E}(q_k)$. Using the least mean square distance to replace M in Eq. (4), the fitting is equivalent to finding the minimum of:

$$S_{\mathrm{MDT}}(D,f)=\int_{\Omega}\sum_{k=1}^{d}\left(E(D,f,q_k)-\hat{E}(q_k)\right)^2 d\Omega, \tag{9}$$

for d different applied gradient directions, and Ω is the image domain with 3D axis (x, y, z). The minimization of Eq. (9) is ill posed, especially in noisy setup, where the summation of different ellipsoids often results in similar spherical profiles [9]. Previous attempts to stabilize the fitting process used geometric constraints such as fixed eigenvalues and multiple restarts [25], or extraction of the fiber orientation with the assumption of two cylindrical symmetric tensors that lie in the same plane [26].

2.2. Multiple diffusion tensors variational framework

The variational-based regularization stabilizes the ill-posed inverse problem of multiple-tensor fitting by adding a smoothness assumption. This assumption follows known facts regarding the diffusion properties of biological samples. These samples are expected, from physiological considerations, to vary in a piece-wise smooth fashion. Therefore, adding a regularization term that pursues piece-wise tensor smoothness, i.e., an edge preserving regularization, should direct the fitting process to the desired result. The framework was previously sketched in Ref. [23] and is fully described next. We apply the regularization via the minimization of the multiple diffusion tensor variational (MDTV) functional:

$$S_{\mathrm{MDTV}}(D,f)=\alpha S_{\mathrm{MDT}}+\int_{\Omega} R(\nabla D)d\Omega. \tag{10}$$

We prefer to achieve tensor smoothness implicitly by separate regularization of the tensor spectrally decomposed elements, via the minimization of

$$S_{\mathrm{MDTV}}(\eta,\lambda,U)=\alpha S_{\mathrm{MDT}}+\int_{\Omega} R(\nabla U,\nabla\lambda,\nabla\eta)d\Omega, \tag{11}$$

with

$$R(\nabla U,\nabla\lambda,\nabla\eta)=\sum_{i=1}^{n}\left(\beta_1\phi_1(||\nabla\eta_i||)+\beta_2\phi_2\left(||\nabla(U_1)_i||\right)+\beta_3\sum_{a=1}^{3}\phi_3\left(||\nabla(\lambda_a)_i||\right)\right) \tag{12}$$

and flow functions φ_i chosen to be $\phi_i(s)=\sqrt{1+s^2/K_i^2}$, which lead to anisotropic diffusion-like flow while preserving discontinuities [16]. The scalars β_1, β_2, β_3 set the relative influence for the regularization of each element. The minimum of Eq. (11) solves the Euler–Lagrange equations and can be found by the gradient descent scheme [see Eqs. (A.1)–(A.4) in Appendix A], which defines a flow

from an initial selection of tensor field parameters $(U)_{[t=0]}$, $(\lambda)_{[t=0]}$, and $(\eta)_{[t=0]}$, until convergence. The minimization is expected to pursue smoothness of fiber orientations (since only the principal orientation U_1 is smoothed), smoothness of fiber shape (by smoothing all eigenvalues) and smoothness of volume fractions over neighboring voxels. Smoothing the spectral elements reduces the problem of tensor flows to scalars and vectors flows. For vector gradient metric, we use the Frobenius norm $||\nabla I|| = \sqrt{\frac{\partial I}{\partial x}\cdot\frac{\partial I}{\partial x}+\frac{\partial I}{\partial y}\cdot\frac{\partial I}{\partial y}+\frac{\partial I}{\partial z}\cdot\frac{\partial I}{\partial z}}$, along with a finite difference scheme to approximate partial derivatives [see Eqs. (B.1)–(B.3) in Appendix B]. The requirement to preserve tensor attributes during the flow is obtained with an orthonormal preserving flow [19], and the explicit eigenvalue access provides a mechanism for control and tuning of biologically driven constraints originating from the expected shape of the fibers. We use this mechanism to regularize the principal eigenvector of the tensors in order to reflect the continuous nature of fibers along neighboring voxels and to enforce anisotropy and positiveness for the fiber compartments.

2.3. Preserving the orthonormal basis

The PDE flow for the principal eigenvectors [see Eq. (A.2) in Appendix A] is initialized with an orthonormal basis, but does not explicitly preserve orthonormality. Changing the principal eigenvector alone, as dictated by the explicit flow, causes loss of orthogonality in relation to the remaining unchanged eigenvectors. The vectors are no longer eigenbasis, spanning the spectral decomposition of a tensor, unless matching changes are performed on the second and third eigenvectors. Preserving the orthonormal basis also demands that the vectors keep their unit length. To resolve both eigenvectors alignment and unit length preservation, we regularize the eigenvectors by simultaneously rotating each set [19]: For each vector basis $(U)_i$, a rotation mechanic momentum vector ω_i is defined as the cross-product of the principal vector with the principal vector change in the explicit flow:

$$\omega_i = (U_1)_i \times \frac{\partial (U_1)_i}{\partial t}. \tag{13}$$

An infinitesimal rotation matrix, Γ_i, corresponding to ω_i, is then computed with the Rodrigues' formula. The flow is defined by the matrix valued PDE:

$$\left((U_a)_i\right)_{[t+\mathrm{dt}]} = \Gamma_i\left((U_a)_i\right)_{[t]}. \tag{14}$$

Applying the flow in Eq. (14) on an initial state of tensors preserves the orthonormal basis during all iterations.

2.4. Eigenvalues monitoring

Controlling the range of eigenvalues is not dictated by the PDE flow derived from Eq. (11), but is desired for diffusion tensor regularization in order to further restrict the minimization into the range of the expected solution. Both eigenvalue monitoring and orthonormality preserving could be added as constraints to the energy function, but this would result in "soft" constraints that are not guaranteed to hold in all iterations. We therefore chose to explicitly monitor these changes. The tensor spectral decomposition provides easy access to eigenvalue manipulation by monitoring the flow in Eq. (A.1) and projecting improper values to the desired range. Eigenvalues determine the shape of the modeled compartment, so we assume that any fiber compartment will follow the cylindrical shape of fibers as an axially symmetric tensor with $\lambda_2=\lambda_3$, and relatively high FA value. Restricting axially symmetric tensors eliminates one parameter for estimation (the smallest eigenvalue) and dictates that the shape of the tensor is determined by the principal eigenvector and two eigenvalues. The remaining eigenvectors can lie anywhere on the plane perpendicular to the principal eigenvector. Therefore, assigning them with an orientation or enforcing smoothness constraints is redundant. For axially symmetric tensors, the ratio $\lambda_2=\lambda_1$ can be determined from a given FA value, $\widetilde{FA}$, as:

$$\frac{\lambda_2}{\lambda_1} = \frac{H}{3-2H}, \tag{15}$$

where H is defined as:

$$H = \frac{\lambda_2}{\langle D\rangle} = 1 - \frac{\widetilde{FA}}{\sqrt{3-2\widetilde{FA}^2}}. \tag{16}$$

The notation $\langle D\rangle$ is reduced to $\langle D\rangle=\lambda_1+2\lambda_2$. The anisotropic threshold is maintained after each iteration by projecting $(\lambda_2)_i>(\lambda_1)_i H/(3-2H)$ to $(\lambda_2)_i=(\lambda_1)_i H/(3-2H)$ for any tensor component i and a threshold $\widetilde{FA} = minFA$. Eigenvalues are also restricted to a range $[min\lambda>0, max\lambda]$. Typical values chosen for thresholds are: $minFA=0.3$, $min\lambda=0.01$ mm^2/s, $max\lambda=4$ mm^2/s. These values are outside the range of expected FA and eigenvalues in white matter [3].

3. Methods

The MDTV framework was implemented in a MATLAB (The MathWorks, Inc., Natick, MA, USA) environment. We have previously demonstrated the separation effect on a phantom of crossing fibers [23], and here we will further analyze the separation capabilities on synthetic datasets created by computer simulations and on a human dataset of a healthy volunteer. In this section, we elaborate on the details of the datasets, selected parameters for the fitting process, and visualization techniques.

3.1. Synthetic data setup

The synthetic datasets consisted of three consecutive slices simulating two fibers crossing. Each slice was 9×9 pixels and the fibers crossed at the center 3×3×3 cube. The setup of the synthetic datasets varied by the angle between the two fibers, by the number of DWI images simulating different applied gradient orientations and by the signal-to-

noise ratio (SNR). The DWIs were assigned with gradient directions chosen by a simulation of symmetric repulsion forces acting on particles spread over the unit sphere. The non-DW image was scaled to 1 at the crossing area. The DWI attenuation was manufactured by substituting the free parameters in Eq. (5) with the following parameters: b=1000 s/mm^2, $(\lambda_1)_i$=1.5×10^{-3} mm^2/s, $(\lambda_2)_i$=$(\lambda_3)_i$=0.4×10^{-3} mm^2/s, $(U)_1$=*eye*(3), $(U)_2$=$\Gamma(U)_1$ for a chosen rotation angle and f_1=f_2=0.5. Rectified white noise was added to the synthesized signal using the following noise simulation:

$$\mathrm{DWI}_{\mathrm{Noisy}} = \sqrt{(\mathrm{DWI} + r_1)^2 + r_2^2}, \tag{17}$$

where r_1 and r_2 are picked from a normal distribution $N(0,\sigma)$. Different datasets were produced with ranging σ values corresponding to the SNR range of 5 to 40. The MDTV framework, MDT fitting and DTI fitting were applied on each dataset and the results were compared. A dataset was given a fitting score for a given method by comparing the fiber orientations found in the nine fiber ambiguous voxels of the middle slice with the expected fiber orientation. The orientation fitting score for each voxel was the mean dot product of the found orientations vs. the expected orientations (equal to 1 if the found orientations were identical to the expected and lower than 1 if otherwise). The score for a dataset was the mean score for the nine voxels. Each experiment consisted of 300 datasets, all with same angle between the fibers, the same number of simulated applied gradients and the same SNR. A score for an experiment was the mean score for the 300 datasets. Two methods applied on the same experiment were compared by counting the number of times one method produced a higher fitting score than the other method, divided by 300.

3.2. Human data setup

MR imaging was performed on a 3-T (GE) MRI system. The diffusion experiments were performed using a DW-EPI sequence with the following parameters: Δ/δ=31/25 ms. The FOV was 22 cm, matrix size was 128×128 and slice thickness was 1.7 mm. Gradient strength was 4 G/cm, resulting in a b value of 1000 s/mm^2 measured in 33 noncollinear gradient directions with four repetitions and 72 axial slices. To avoid intrinsic pulsative brain motion artifact, the sequence was gated to the cardiac cycle with effective TR of 30 R-R intervals and TE of 88 ms. The DWIs were corrected for motion using SPM2 software (UCL, London, UK). Gradient orientations were compensated to account for any rotation applied to the DWIs. The local institutional review board committee approved the MRI protocol and informed consent was obtained from subjects.

3.3. Data fitting and parameters

The MDTV and MDT data fitting were achieved by minimization of the functional Eq. (11). We restricted β_1=β_2=β_3=0 for MDT fitting, which reduced the functional to Eq. (9). DTI results were acquired by least mean squares linear approximation. Initial guesses for the minimization were generated in the following way: DTI results were calculated and the fitting error in each voxel was determined as the least mean square distance from the signal. The resulting tensors were spectrally decomposed, and the eigenvalues were replaced with chosen anisotropic eigenvalues, e.g., [1.5 0.4 0.4]. The new tensors were duplicated to create two identical components, following which a random rotation was applied on each tensor. The rotation was performed using Eq. (14) with a momentum (dt) proportional to the DTI fitting error. The relative normalized weights, η_1 and η_2, were initialized to 0, i.e., f_1=f_2=0.5. The fitting was terminated after 400 iterations. Implementation with MATLAB was chosen for simplicity yet with the price of highly inefficient and time-consuming methods (5 min per iteration for the human dataset on an AMD opteron-250 desktop). The values of the K parameters tune the anisotropic behavior of the φ functions. They determine the probability for a given value difference to be treated as an edge to be preserved. Setting the parameters is influenced by the expected range of η, U and λ, and by an observer perception of important edges. For the

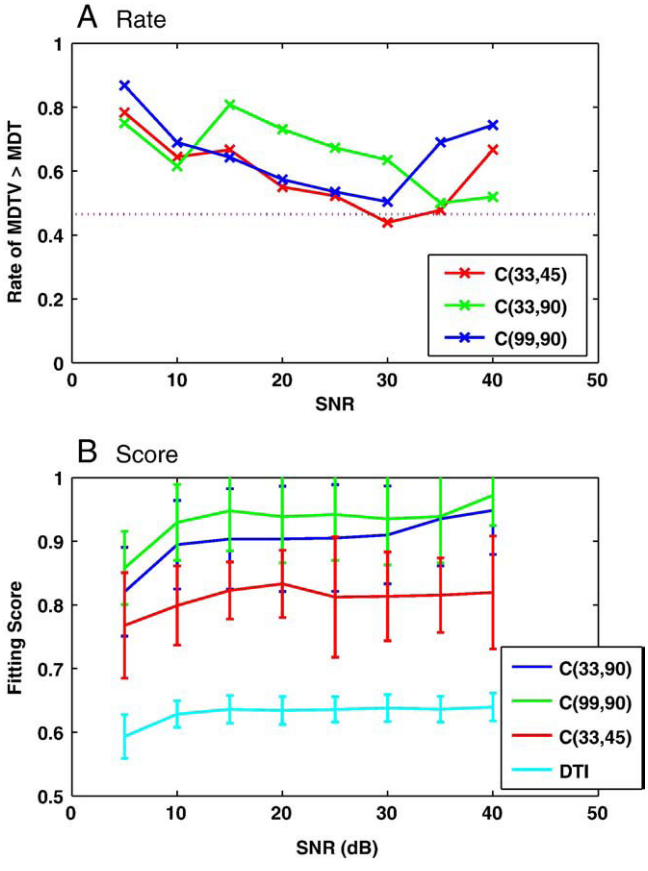

Fig. 1. Synthetic data. The rate of better MDTV results than MDT (A) results for varying experiments and SNR shows that, for most experiments, MDTV provided better results than MDT (>0.5) and that as SNR decreased the rate tended to increase. The fitting error for MDTV experiments (B) shows that the score depended on the experimental conditions.

type of data we expect in brain imaging, we find the following parameters satisfying: K_1=0.25, K_2=0.1, K_3=0.1. The relative regularization weights were α=1 and β_1=0.02, β_2=0.05, β_3=0.05. The ratio between α and β determines the amount of smoothing that will be performed and again is influenced by the perception of important edges. The ratio between the different β values determines the relative speed of each parameter convergence; optimized selection reduces the total convergence time.

3.4. Visualization

Principal vector fields are presented as a color-coded image, with the principal vector components denoted as red, green and blue values attenuated by FA [27]. Ellipsoid visualization is used for multiple-tensor fields: each tensor is assigned an ellipsoid 3D object, colored according to the color-code scheme. Ellipsoid size is scaled by the relative weight.

The tractography images were produced using an in-house program, and the resulting tracts were visualized using MATLAB's "streamline" function. For DTI, the tracts were produced by brute-force FACT method [28], following the principal orientation starting from each voxel in the brain. The tracking advances in both symmetric directions, with subvoxel steps (0.1×voxel size), and was terminated at voxels with FA lower than a threshold (typically 0.25). Each step is made in the direction indicated by the vector representing the current voxel. Finally, a set of regions of interest (ROIs) are manually selected according to anatomical landmarks. The ROI set restricts areas where the fibers have to pass or are not allowed to pass. Only tracts that agree with the set of constraints are plotted. A simple variation of the tractography technique described above was used in order to plot tracts out of the MDTV vector field: each voxel is represented by up to two vectors, providing two possible tracts from the same voxel. We then chose the vector creating the smallest angle with the previously found tract. In this process, only vectors representing tensors with a relative weight higher than 0.3 were used. The tracking stops when arriving at a voxel where both tensors have FA lower than a threshold (this threshold has to be higher than *minFA*).

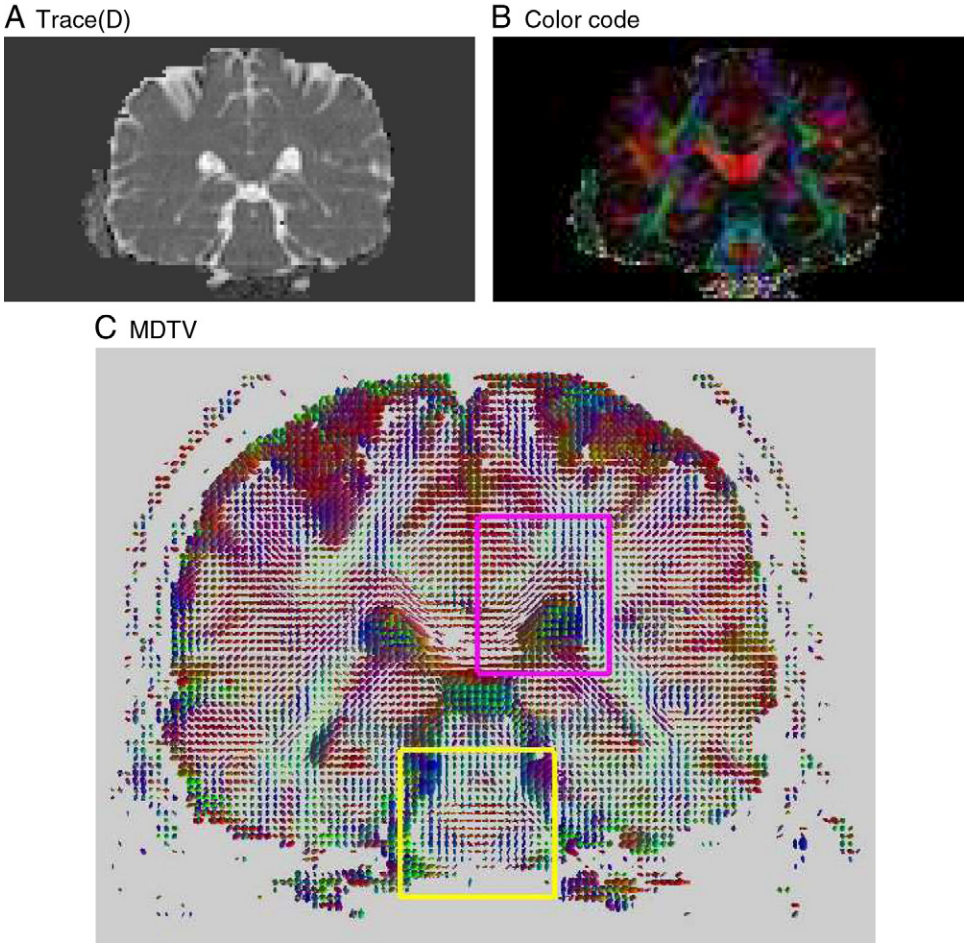

Fig. 2. Coronal slice. The ellipsoid visualization of the MDTV resultant tensor field (C) delineated white matter tracts, including intersections, and showed a difference between CSF and brain tissue. The pons and corpus callosum ROIs are marked with rectangles. Image of *Trace*(*D*) (A) and color-coded image (B) for the DTI analysis are shown as anatomical references.

4. Results

We examined the framework abilities in a synthetic setup with varying parameters. We compared MDTV results for the synthetic experiment with MDT results for the same experiments. We concluded by applying the MDTV framework to the human brain dataset, with attention focused on brain areas known to have crossing fibers.

4.1. Synthetic data

The synthetic data simulations investigated MDT and MDTV fitting for SNR varying datasets, for a varying number of applied gradient orientations and for varying angles between two simulated fibers. We used the notation $C(d,\theta)$ for an experiment with d diffusion directions and fibers aligned with an angle θ. We compared the fitting results for the experiments $C(99,90)$, $C(33,90)$ and $C(33,45)$. Fig. 1A plots the rate of better MDTV results for varying SNR values as calculated for the different experiments. Most entries were larger than 0.5, which means that in most cases MDTV provided better fitting orientations than MDT. The plot further showed that as SNR decreased the rate of better MDTV results increased. Fig. 1B shows the fitting score for the different MDTV experiments: The trends of the plot show that the score increased if the gradient number increased, if SNR increased and if the angle got closer to 90°. The synthetic data results suggest that as the conditions of the experiment got worse, i.e., noisier, with less applied gradient directions or with closer aligned fibers, the performance of MDTV was reduced, but at the same time, the percentage of better MDTV results than MDT was increased. A possible explanation is that MDT fitting is more sensitive to the design of the experiment than MDTV fitting.

4.2. Human data

We present a single coronal slice from the human dataset that demonstrates the performance of the MDTV framework. Fig. 2 shows *Trace*(*D*) and color-coded images for the DTI analysis as anatomical landmarks, together with the ellipsoid visualization for the MDTV resultant multiple-tensor field. Unlike the synthetic data, which can be addressed as "ground truth," the fiber orientations and diffusivity in the brain data are not known. Although large fiber bundles have common shapes and expected tracts, the shapes are still dependent on the exact orientation of the subject relative to the scanner and, of course, on the age and physical condition of the subject. Thus, the results can be verified only by visually comparing relatively known fiber bundles with other atlas examples. The human dataset differs from the synthetic and phantom datasets in that many voxels in the human dataset contain nonfiber tissue (CSF or gray matter). In these voxels, other types of partial volume effects (such as gray/white matter interface and CSF contamination) may occur. The MDTV model does not account for these effects. The slice presented is slightly posterior to mid-coronal (slice 77 out of 128) and was selected to include the pons, where the middle cerebellar peduncle (mcp) tract crosses the bundle of the corticospinal tracts (cst) and the corticopontine tract (cpt) [29]. The ROI is denoted by a yellow rectangle. In Fig. 3, the zoomed DTI color map and the MDTV ellipsoid visualization images of the ROI are presented. Within the pons, we see the transverse pontine fibers (tpf), which are a part of the mcp, that cross the midline

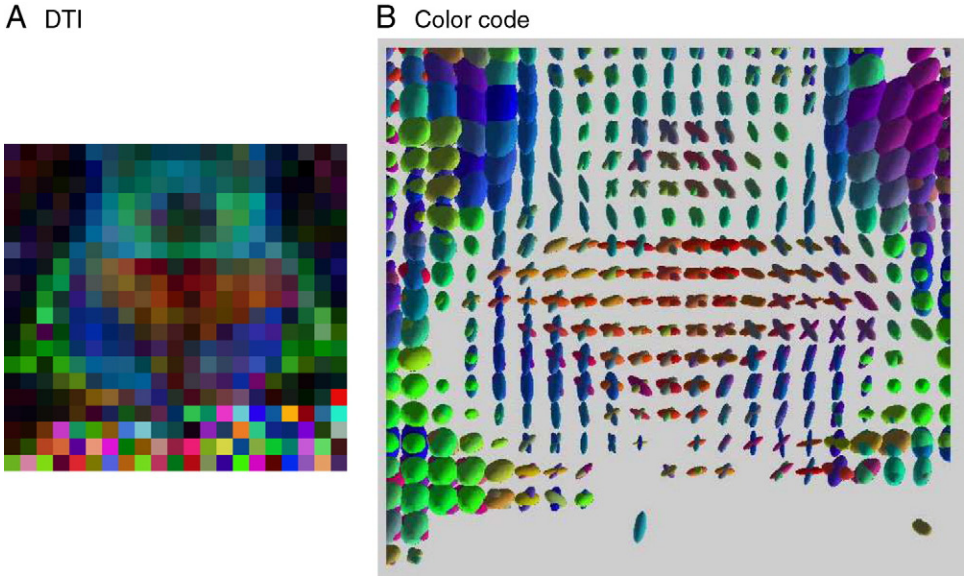

Fig. 3. Pons. The DTI color code (A) shows the transverse pontine fibers in red and the corticospinal tracts in blue. The ellipsoid visualization for MDTV (B) shows the intersection between those fibers. Because ellipsoid sizes are weighted by their relative volume fraction, when f approaches 0.5 there are two components visible, and when f decreases, its ellipsoid visually disappears.

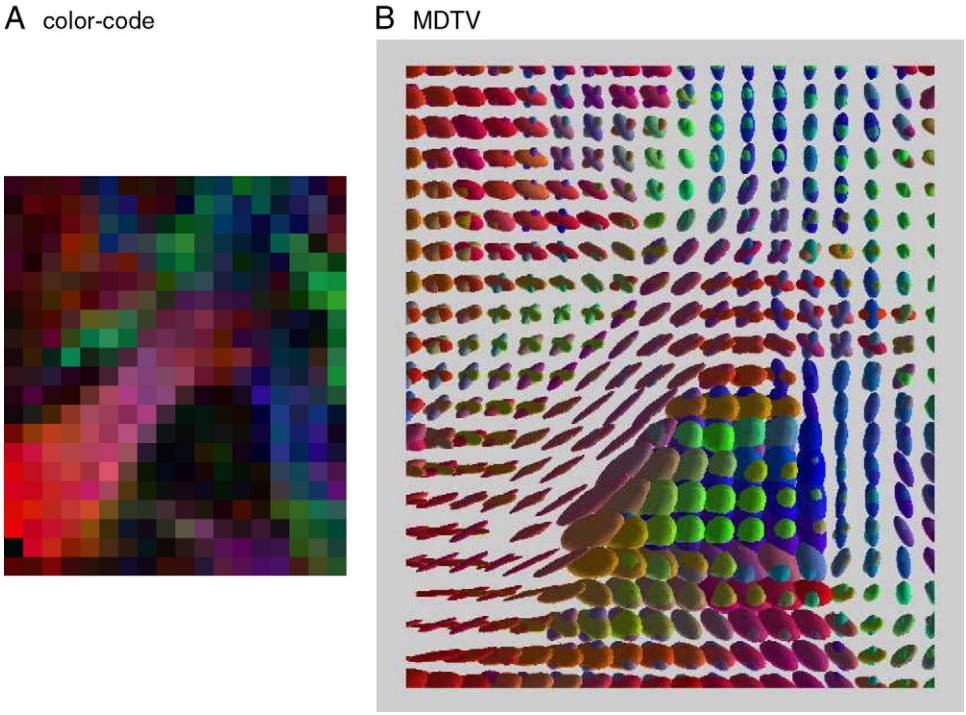

Fig. 4. Corpus callosum. The DTI color code (A) shows the corpus callosum in red and the corticospinal tracts in blue. The intersection area is black due to low FA. The ellipsoid visualization for MDTV (B) shows a single component for the genu of the corpus callosum with a second component in the area of intersection.

in a left–right direction and are colored red. In the slice selected, the tpf intersects the cst in an inferior–superior oriented, blue-colored bundle. All voxels were fitted to two tensors, but since the visualization weighs the ellipsoids by their relative volume, it appears in many voxels as if only a single tensor was found; these voxels are usually areas with a single organized white matter bundle. Two ellipsoids in the same voxel are visible as the volume fraction approaches 0.5. The ellipsoid visualization shows that in the expected areas for the tpf and cst crossing, there are two visible fiber components (elongated ellipsoids): one with left–right orientation and the other with inferior–superior orientation. Those ellipsoids continue the trajectories of the cst and tpf from neighboring, single-fiber population voxels. A second ROI on the same coronal slice, marked with a magenta rectangle, is superior to the previous ROI and shows the left–right oriented corpus callosum (cc) intersection with inferior–superior fiber bundle consisting of the cst, the cpt and the superior thalamic radiation [29]. The enlarged area is presented in Fig. 4. The MDTV ellipsoid visualization shows a single component at the closer-to-midline parts of the genu of the cc, and as the tract gets further from the midline and closer to the cst bundle, a second component of blue inferior–superior ellipsoids is found. This ROI nicely demonstrated the ability of MDTV to recognize areas of single fibers, as seen in the genu of the cc. This area is visualized either as a single ellipsoid or two very similar ellipsoids.

Since the pyramidal tracts converge and cross in many points along the path between the spinal cord and the cortex, there are many points of ambiguity, where tractography methods are prone to fail. Indeed, trying to delineate the pyramidal tracts produces only partial reconstruction of the whole tract (Fig. 5A). These tracts were selected by placing two axially positioned seed ROIs (shown in green), one at the dorsal part of the brain superior to the corpus callosum, and the other at the ventral part. Both seed ROIs cover an entire hemisphere and restrict the presentation only to fibers that cross through that hemisphere along the expected path of the pyramidal tract. Two additional restricting ROIs were used to eliminate fibers that cross to the opposite hemisphere. For DTI, only a sketch of the main route of the fiber is found, as a result many cortical areas known to be connected with the lower brain parts were not delineated. Using the same ROI restrictions for the MDTV database reveals a much more complete view of the fiber (Fig. 5B), connecting many more cortical areas and resembling the expected shape of the tract.

5. Discussion

The MDTV framework was designed for fitting of fiber-ambiguous voxels. However, since there is no restriction on the volume fraction parameter (other than positivity), the fitting was also successful in areas of a single fiber. The fitted two components are either identical in shape with different volume fractions, or there is one component with a dominant volume fraction that best describes the data; the remaining

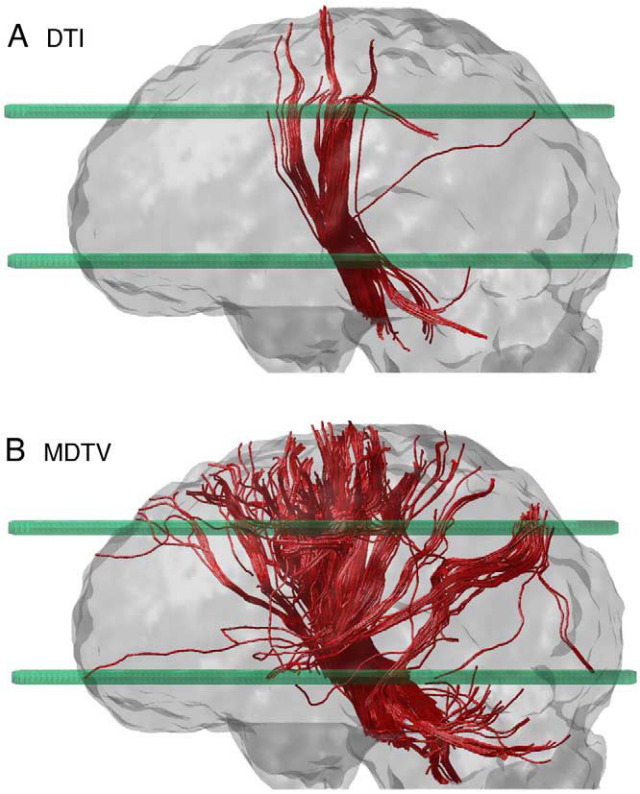

Fig. 5. Tractography. The pyramidal tract was obtained by selecting all fibers that pass in both seed ROIs (green surfaces). The MDTV fiber (B) is much more complete than the DTI fiber (A), connecting larger parts of the cortex with the brainstem. This suggests that fiber ambiguity causes pretermination of tracts.

low-volume component is expected to model the fitting residual. Visually, the low-volume component disappears in the ellipsoid visualization. It can be further eliminated from any post-processing (such as tractography) by introducing a threshold on the minimal volume fraction value.

The MDTV minimization dictates the minimal FA (*FAmin*) that can be obtained for each tensor. This restriction is sensible for white matter areas, but is certainly questionable for CSF and gray matter areas. Best results will therefore be achieved by applying the MDTV framework only on segmented white matter voxels. Moreover, since MDTV is expected to find similar fiber orientations to DTI in single-fiber voxels, results could be further improved by applying the MDTV framework only on voxels suspected of having more than one component; DTI results could be used in the remaining voxels. This should restrict the MDTV analysis to a much smaller number of voxels and decrease runtime. We applied the minimization on the complete human dataset here, without pre-segmentation of white matter, anticipating poor fitting in CSF or gray matter areas. Despite the fact that only anisotropic tensors were fitted to the data, the ellipsoid visualization clearly shows the difference between isotropic CSF area and the rest of the brain. In isotropic CSF areas, the fitting resulted in two anisotropic tensors which, together, visually resemble an isotropic tensor. We therefore suggest that, in multiple-tensor analysis, the use of FA as white matter segmentation threshold or tractography stopping criteria is too inclusive. FA-based tissue segmentation might result in misidentification of isotropic tissue as neuronal fiber.

Fig. 6 shows voxels whose convergence was constrained by the minimal FA. Red voxels are those in which only one of the components reached the threshold, and green voxels are those in which both components reached the threshold. The voxels nicely segment the CSF, evidenced by comparing the *T*1 image resliced with the DWI image domain. The fitting did not reach the minimal FA threshold in the rest of the brain. Red voxels seem to occur mainly in the interface between white matter and the CSF, leading us to speculate that we should be able to reduce the partial volume effect within an isotropic compartment by adjusting the minimal FA thresholds, restricting one component to be isotropic and the other anisotropic. This type of partial volume occurs in cases such as CSF contamination and edematous tissue (see Ref. [30] for preliminary results). We also note that voxels expected to be occupied by white matter did not reach the minimal FA threshold, and therefore their obtained FA values

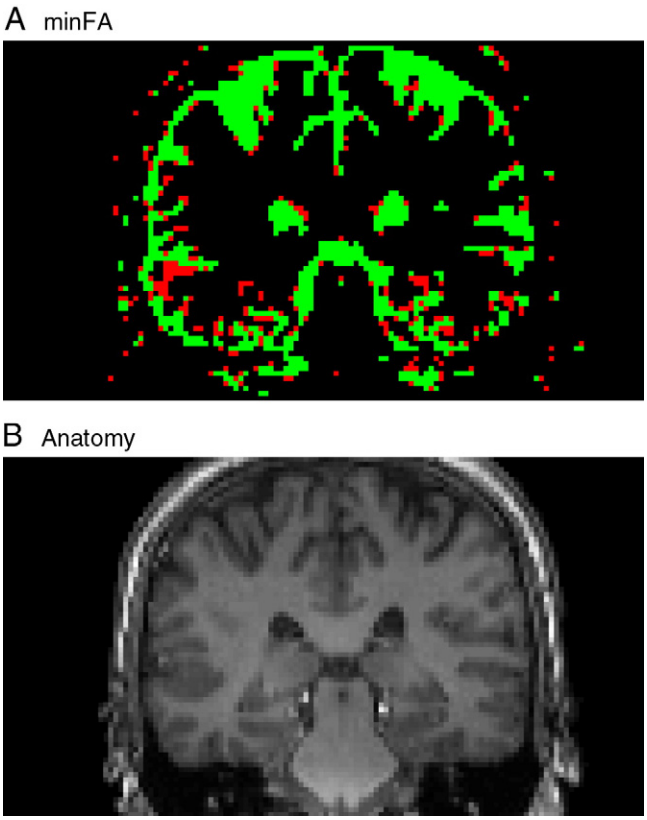

Fig. 6. FA threshold. FA was constrained by a minimal threshold. (A) Voxels that reach the threshold at the final iteration. Red indicates that only one component reached the threshold, and green that both reached the threshold. The colored voxels match the CSF in a realigned T1 image (B). The red voxels appear to be in CSF-contaminated voxels.

(one for each component) can be considered a good tissue anisotropy description.

We have used the findings that gray matter and CSF voxels converge to the minimal FA threshold for setting the tractography stopping criteria. This was set to a higher FA value than the minimal FA and was combined with a minimal volume fraction threshold. Such a stopping criteria seems adequate for the FACT algorithm, providing us with better fiber delineation. However, it is important to note that the correctness of tractography results suffers from other artifacts, such as noise, resolution and other algorithm-dependent inaccuracies. Nevertheless, it is our belief that using regularization and better modeling should increase the stability and correctness of the FACT algorithm. This issue should be better inspected, along with the question of how other tractography algorithms are influenced.

A second threshold used in the minimization process is for minimal eigenvalues. This threshold eliminates the possibility of negative eigenvalues as fitting results. Although not physically possible, voxels with negative eigenvalues are often found in brain scans; we therefore identified voxels with high probability to have negative eigenvalues and eliminated them from any further analysis. This elimination was done by throwing out any voxel with a normalized signal of 0 or larger than 1 in any of the normalized DWIs (such voxels appear as white spaces in the ellipsoid visualization). We note that none of the remaining voxels had an eigenvalue that came near the minimal eigenvalue chosen.

The addition of regularization terms in the variational framework stabilizes the minimization process, but does not prevent local minima entrapment. This is a problem shared by all variational methods when the functional is not convex. Additional regularization terms and smart initialization should reduce the chance of falling in local minima. As mentioned above, the performance could be enhanced by introducing a priory structural information such as tissue segmentation [20,31]. Another improvement for the regularization may come from incorporating tensor-based PDE flows [32–34]. These are more natural for handling tensors, but adding anisotropy constraints to such flows remains to be investigated.

Another issue that affects the quality of fit is the selection of the model. In a previous study [23], we have shown that denoising alone, or any other image enhancement for that matter, cannot assign correct orientations for more than one fiber per voxel as long as the DTI model is the model to be fitted. Since MDTV relies on the multiple-tensor model, it can assign more than one orientation for each voxel, and the recovery of two fiber directions is made possible. The assumptions behind the MDT model are that any compartment is completely separated from all other compartments, and that the diffusion within each compartment is homogenous and not restricted. Contrary to this assumption, there are evidences that diffusion within fibers is restricted [35]. The use of higher b values was proposed as a way to amplify the orientational heterogeneity in multiple compartment voxels [36], and models that take into account the restricted component were shown to resolve fiber ambiguity [10]. We assume that applying the MDTV data on higher b value data will yield better fitting results, although the validity of the tensor model for higher b values is questionable. The number of fitted components is limited to two by experiments presented here, and the stability of the fitting for higher numbers of components remains to be determined. The MDTV framework described here lays down the map for variational frameworks for other model-based methods and, with the correct selection of regularization terms, parameters and initialization, should produce better results than conventional fitting procedures.

6. Summary and conclusions

The MDTV framework demonstrated that variational model regularization is helpful in solving the ill-posed inverse problem of multiple-tensor fit. The synthetic data results suggest that the MDTV framework can resolve fiber ambiguity of two crossing fibers within the same voxel, with better separation than the nonregularized MDT model, for a wide range of noise levels. Combining the MDTV approach with existing tractography techniques provides better nerve bundle delineations in homogenous areas and especially in partial volume, fiber-ambiguous areas. We have demonstrated the MDTV framework fitting on human data and shown intersections in areas that are anatomically known to have crossing fibers. Using the outcome tensor field of the MDTV framework should improve the accuracy of any further processing, allowing new insights to brain architecture. Modifying the framework to account for other partial volume effects, or other diffusion models, may increase the accuracy of brain tissue diffusion imaging even further.

Acknowledgment

We acknowledge the support of the Functional Brain Imaging Unit, The Wohl Institute for Advanced Imaging; Tel Aviv-Sourasky Medical Center and Tel Aviv University; The Adams Super-Center for Brain Research of Tel Aviv University; The Israel Academy of Sciences; Israel Ministry of Science; and the Tel Aviv University Research Authority.

Appendix A. Gradient descent scheme for MDTV

The minimum of Eq. (11) solves the Euler–Lagrange equations. We find it by the gradient descent scheme. The result is a system of coupled diffusion-like equations. The equations for the eigenvalues are

$$\frac{\partial (\lambda_a)_i}{\partial t} = 2\alpha b \sum_{k=1}^{d} \left(F(q_k) f_i E_i(k) \left(q_k^{\mathrm{T}} (U_a)_i (U_a)_i^T q_k \right) \right) + \beta_3 \mathrm{div} \left(\frac{\varphi'_3 \left(|\nabla (\lambda_a)_i| \right)}{|\nabla (\lambda_a)_i|} \nabla (\lambda_a)_i \right), \quad \text{(A.1)}$$

where $F(q_k) = E(q_k) - \hat{E}(q_k)$. Those for the eigenvectors have the following form:

$$\frac{\partial \left(U_1^j\right)_i}{\partial t} = 2\alpha b \sum_{k=1}^{d} \left(F(q_k) f_i E_i(k) \lambda_i^1(q_k)_j \left(q_k \cdot (U_1)_i\right)\right) + \beta_2 \mathrm{div}\left(\frac{\varphi'_2\left(\left|\nabla \left(U_1^j\right)_i\right|\right)}{\left|\nabla \left(U_1^j\right)_i\right|} \nabla \left(U_1^j\right)_i \right), \tag{A.2}$$

where $(U_1^j)_i$ is the jth component of the vector $(U_1)_i$ and $(q_k)_j$ is the jth component of the vector q_k. Finally, we obtain the equations for the weights:

$$\frac{\partial \eta_i}{\partial t} = -2\alpha_1 \frac{e^{\eta_i}}{\left(\sum_{j=1}^{n} e^{\eta_i}\right)^2} \times \sum_{k=1}^{d} F(q_k) \left(\sum_j \left(1-\delta_{ij}\right)\left(E_i(q_k) - E_j(q_k) e^{\eta_j}\right)\right) + \beta_1 \mathrm{div}\left(\frac{\varphi'_1\left(\left|\nabla \eta_i\right|\right)}{\left|\nabla \eta_i\right|} \nabla \eta_i \right), \tag{A.3}$$

where δ_{ij}=1 if i=j and 0 otherwise. For all the parameters, we use Neumann boundary condition, and the initial conditions for any parameter X are

$$(X)_{[t=0]} = (X)_{[0]}. \tag{A.4}$$

Appendix B. Finite difference for symmetric vectors

We approximate the calculation of gradients with a finite difference scheme. Calculation of $|\nabla(U_1)_i|$ requires that the finite difference scheme take into account the symmetric properties of diffusion orientations. Since the MR signal decay is influenced by self-diffusion along both directions of the applied gradient, the choice between $(U_1)_i$ to $-(U_1)_i$ is arbitrary. However, measuring the variation between vectors according to the Euclidian distance depends on the sign chosen. Therefore, the distance from a vector to its neighbor is computed after locally inverting neighboring vectors [19], i.e., flipping signs, to create a sharp angle with the chosen vector. The finite difference scheme for a vector field I with 3D domain axes x, y and z for approximating partial derivatives over axis x is:

$$\mathrm{flip}_1 = \mathrm{sign}(I(x+1,y,z) \cdot I(x-1,y,z)) \ .$$

$$\mathrm{flip}_2 = \mathrm{sign}((\mathrm{flip}_1 I(x+1,y,z) + I(x-1,y,z)) \cdot I(x,y,z))$$

$$\mathrm{flip}_3 = \mathrm{sign}(I(x,y+1,z) \cdot I(x,y-1,z))$$

$$\mathrm{flip}_4 = \mathrm{sign}((\mathrm{flip}_1 I(x+1,y,z) - I(x-1,y,z)) \cdot (\mathrm{flip}_3 I(x,y-1,z) - I(x,y+1,z)))$$

$$\frac{\partial I(x,y,z)}{\partial x} = \frac{\mathrm{flip}_1 I(x+1,y,z) - I(x-1,y,z)}{2\hat{x}}. \tag{B.1}$$

$$\frac{\partial I(x,y,z)}{\partial^2 x} = \frac{\mathrm{flip}_2(\mathrm{flip}_1 I(x+1,y,z) + I(x-1,y,z)) - 2I(x,y,z)}{\hat{x}^2}. \tag{B.2}$$

$$\frac{\partial I(x,y,z)}{\partial x \partial y} = \frac{\mathrm{flip}_4(\mathrm{flip}_1 I(x+1,y,z) - I(x-1,y,z))}{4\hat{x}\hat{y}} + \frac{\mathrm{flip}_3 I(x,y-1,z) - I(x,y+1,z)}{4\hat{x}\hat{y}}. \tag{B.3}$$

The voxel size proportions are $\hat{x}$, $\hat{y}$ and $\hat{z}$. By permuting x, y and z in Eqs. (B.1), (B.2) and (B.3), the entire scheme is defined.

References

[1] Stejskal E, Tanner JE. Spin diffusion measurements: spin echoes in the presence of a time-dependant field gradient. J Chem Phys 1965;42:288–92.

[2] Basser PJ, Mattiello J, Le-Bihan D. MR Diffusion tensor spectroscopy and imaging. Biophys J 1994;66:259–67.

[3] Pierpaoli C, Jezzard P, Basser PJ, Barnett A, Di-Chiro G. Diffusion tensor MR imaging of human brain. Radiology 1996;201:637–48.

[4] Le-Bihan D, Breton E, Lallemand D, Grenier P, Cabanis E, Laval-Jeantet M. MR Imaging of intravoxel incoherent motions: application to diffusion and perfusion in neurologic disorders. Radiology 1986;161:401–7.

[5] Basser PJ, Pierpaoli C. Microstructural and physiological features of tissues elucidated by quantitative-diffusion-tensor MRI. J Magn Reson Imaging 1996;111(3):209–19.

[6] Basser PJ, Pajevic S, Pierpaoli C, Duda J, Aldroubi A. In vivo fiber tractography using DT-MRI data. Magn Reson Med 2000;44:625–32.

[7] Pierpaoli C, Basser PJ. Toward a quantitative assessment of diffusion anisotropy. Magn Reson Med 1996;36(6):893–906.

[8] Alexander AL, Hasan KM, Lazar M, Tsuruda JS, Parker DL. Analysis of partial volume effects in diffusion-tensor MRI. Magn Reson Med 2001;45(5):770–80.

[9] Alexander DC, Barker GJ, Arridge SR. Detection and modeling of non-Gaussian apparent diffusion coefficient profiles in human brain data. Magn Reson Med 2002;48:331–40.

[10] Assaf Y, Freidlin RZ, Rohde GK, Basser PJ. New modeling and experimental framework to characterize hindered and restricted water diffusion in brain white matter. Magn Reson Med 2004;52:965–78.

[11] Tuch DS, Reese TG, Wiegell MR, Wedeen Van J. Diffusion MRI of complex neural architecture. Neuron 2003;40:885–95.

[12] Tournier JD, Calamante F, Gadian DG, Connelly A. Direct estimation of the fiber orientation density function from diffusion-weighted MRI data using spherical deconvolution. NeuroImage 2004;23:1176–85.

[13] Ozarslan E, Mareci TH. Generalized diffusion tensor imaging and analytical relationships between diffusion tensor imaging and high angular resolution diffusion imaging. Magn Reson Med 2003;50(5):955–65.

[14] Jansons KM, Alexander DC. Persistent angular structure: new insights from diffusion MRI data. Inverse Probl 2003;19:1031–46.

[15] Alexander DC. Multiple-fibre reconstruction algorithms for diffusion MRI. Ann N Y Acad Sci 2005;1046:113–33.

[16] Aubert G, Kornprobst P. Mathematical problems in image processing: partial differential equations and the calculus of variations. Applied Mathematical Sciences, vol. 147. New York: Springer-Verlag; 2002.

[17] Parker GJM, Schnabel JA, Symms MR, Werring DJ, Garker GJ. Nonlinear smoothing for reduction of systematic and random errors in diffusion tensor imaging. J Magn Reson Imaging 2000;11(6):702–10.

[18] Vemuri BC, Chen Y, Rao M, McGraw T, Wang Z, Mareci T. Fiber tract mapping from diffusion tensor MRI. In: Proc IEEE Workshop Variational and Level Set Methods in Computer Vision; 2001. p. 81–8.

[19] Tschumperlé D, Deriche R. Orthonormal vector sets regularization with PDE's and applications. Int J Comput Vis 2002;50(3):237–52.
[20] Coulon O, Alexander DC, Arridge SR. A regularization scheme for diffusion tensor magnetic resonance images. IPMI'01. London, UK: Springer-Verlag; 2001. p. 92–105.
[21] Tschumperlé D, Deriche R. Variational frameworks for DT-MRI estimation, regularization and visualization. In: Proc of the 9th International Conference on Computer Vision, Nice, France; 2003. p. 116–21.
[22] Wang Z, Vemuri BC, Chen Y, Mareci TH. A constrained variational principle for direct estimation and smoothing of the diffusion tensor field from complex DWI. IEEE Trans Med Imaging 2004;23(8):930–9.
[23] Pasternak O, Sochen N, Assaf Y. Variational regularization of multiple diffusion tensor fields. In: Weickert J, Hagen H, editors. Visualization and Processing of Tensor Fields. Berlin: Springer; 2006. p. 165–76.
[24] Ramirez-Manzanares A, Rivera M. Basis tensor decomposition for restoring intra-voxel structure and stochastic walks for inferring brain connectivity in DT-MRI. Int J Comput Vis 2006;69(1):77–92.
[25] Tuch DS, Reese TG, Wiegell MR, Makris NG, Belliveau JW, Wedeen VJ. High angular resolution diffusion imaging reveals intravoxel white matter fiber heterogeneity. Magn Reson Med 2002;48:577–82.
[26] Peled S, Friman O, Jolesz F, Westin CF. Geometrically constrained two-tensor model for crossing tracts in DWI. Magn Reson Imaging 2006;24:1263–70.
[27] Pajevic S, Pierpaoli C. Color schemes to represent the orientation of anisotropic tissues from diffusion tensor data: application to white matter fiber tract mapping in the human brain. Magn Reson Med 1999; 42:526–40.
[28] Mori S, Crain BJ, Chacko VP, Van Zijl PCM. Three dimensional tracking of axonal projections in the brain by magnetic resonance imaging. Ann Neurol 1999;45:265–9.
[29] Mori S, Wakana S, Nagae-Poetscher LM, van Zijl PCM. MRI Atlas of human white matter. Amsterdam: Elsevier; 2005.
[30] Pasternak O, Sochen N, Intrator N, Assaf Y. Neuronal fiber delineation in area of edema from diffusion weighted MRI. In: Proc Neural Information Processing Systems; 2005.
[31] Weickert J. Coherence enhancing diffusion filtering. Int J Comput Vis 1999;31(2/3):111–27.
[32] Gur Y, Pasternak O, Sochen N. Fast invariant Riemannian DT-MRI regularization. In: Proc Mathematical Methods in Biomedical Image Analysis; 2007.
[33] Pennec X, Fillard P, Ayache N. A Riemannian framework for tensor computing. Int J Comput Vis 2006;66(1):41–66.
[34] Lenglet C, Rousson M, Deriche R, Faugeras O. Statistics on the manifold of multivariate normal distributions: theory and application to diffusion tensor MRI processing. J Math Imaging Vision 2006;25(3): 423–44.
[35] Callaghan PT. Principles of nuclear magnetic resonance microscopy. Great Britain: Oxford; 1993.
[36] Alexander DC, Barker GJ. Optimal imaging parameters for fiber-orientation estimation in diffusion MRI. NeuroImage 2005;27: 357–67.